

# Dual atomic catalysts from COF-derived carbon for CO<sub>2</sub>RR by suppressing HER through synergistic effects

Minghao Liu<sup>1,2</sup> | Sijia Liu<sup>1</sup> | Qing Xu<sup>1,3</sup>  | Qiyang Miao<sup>1</sup> | Shuai Yang<sup>3,4</sup> | Svenja Hanson<sup>2</sup> | George Zheng Chen<sup>5</sup> | Jun He<sup>2</sup> | Zheng Jiang<sup>3,4</sup> | Gaofeng Zeng<sup>1,3</sup>

<sup>1</sup>CAS Key Laboratory of Low-Carbon Conversion Science and Engineering, Shanghai Advanced Research Institute (SARI), Chinese Academy of Sciences (CAS), Shanghai, People's Republic of China

<sup>2</sup>Department of Chemical and Environmental Engineering, University of Nottingham Ningbo China, Ningbo, People's Republic of China

<sup>3</sup>School of Chemical Engineering, University of Chinese Academy of Sciences, Beijing, People's Republic of China

<sup>4</sup>Shanghai Synchrotron Radiation Facility, Shanghai Advanced Research Institute, Chinese Academy of Science, Shanghai, People's Republic of China

<sup>5</sup>Department of Chemical and Environmental Engineering, University of Nottingham, Nottingham, UK

## Correspondence

Qing Xu and Gaofeng Zeng, CAS Key Laboratory of Low-Carbon Conversion Science and Engineering, Shanghai Advanced Research Institute (SARI), Chinese Academy of Sciences (CAS), 201210 Shanghai, People's Republic of China.

Email: [xuqing@sari.ac.cn](mailto:xuqing@sari.ac.cn) and [zenggf@sari.ac.cn](mailto:zenggf@sari.ac.cn)

Jun He, Department of Chemical and Environmental Engineering, University of Nottingham Ningbo China, 315199 Ningbo, People's Republic of China. Email: [Jun.He@nottingham.edu.cn](mailto:Jun.He@nottingham.edu.cn)

## Abstract

The electrochemical carbon dioxide reduction reaction (CO<sub>2</sub>RR) for high-value-added products is a promising strategy to tackle excessive CO<sub>2</sub> emissions. However, the activity of and selectivity for catalysts for CO<sub>2</sub>RR still need to be improved because of the competing reaction (hydrogen evolution reaction). In this study, for the first time, we have demonstrated dual atomic catalytic sites for CO<sub>2</sub>RR from a core-shell hybrid of the covalent-organic framework and the metal-organic framework. Due to abundant dual atomic sites (with CoN<sub>4</sub>O and ZnN<sub>4</sub> of 2.47 and 11.05 wt.%, respectively) on hollow carbon, the catalyst promoted catalysis of CO<sub>2</sub>RR, with the highest Faradic efficiency for CO of 92.6% at -0.8 V and a turnover frequency value of 1370.24 h<sup>-1</sup> at -1.0 V. More importantly, the activity and selectivity of the catalyst were well retained for 30 h. The theoretical calculation further revealed that CoN<sub>4</sub>O was the main site for CO<sub>2</sub>RR, and the activity of and selectivity for Zn sites were also improved because of the synergetic roles.

## KEYWORDS

carbon dioxide reduction reaction, covalent-organic frameworks, dual atomic catalysts, metal-organic frameworks, single-atom catalysts

Minghao Liu and Sijia Liu contributed equally to this study.

This is an open access article under the terms of the Creative Commons Attribution License, which permits use, distribution and reproduction in any medium, provided the original work is properly cited.

© 2023 The Authors. *Carbon Energy* published by Wenzhou University and John Wiley & Sons Australia, Ltd.

## 1 | INTRODUCTION

Electrocatalytic CO<sub>2</sub> reduction reaction (CO<sub>2</sub>RR) for high-value chemicals is a promising method to curb CO<sub>2</sub> emissions and alleviate the energy crisis.<sup>1–7</sup> Developing catalysts with high activity, selectivity, and stability is a major challenge due to the competing hydrogen evolution reaction (HER) in the catalytic process.<sup>8–11</sup> With the rapid development of catalysts for CO<sub>2</sub>RR, various electrocatalysts have been studied, such as molecular (e.g., Ni<sub>4</sub>FeS<sub>4</sub>), metal-free carbon-based (e.g., NCNTs), single-atom (e.g., NiSA-N-CNTs), and metal-based (e.g., alloys and oxides) electrocatalysts.<sup>12–18</sup> Among them, carbon-supported single-atom catalysts (SACs) are receiving more attention due to the designable catalytic centers and tunable supports.<sup>19–26</sup> Introducing a new kind of metal atom into SACs to form bimetallic catalytic sites is an effective method to improve the catalytic performance of the CO<sub>2</sub>RRs.<sup>27–32</sup> However, it still remains a challenge to confer synergetic roles for the different metal atoms in the same supports because of the long distances between isolated active sites.<sup>33–35</sup> To overcome the weak interaction between isolated atoms, the heteroatom modulator approach, the ball-milling method, atomic layer deposition, and template-pyrolysis strategies have been used to construct dual sites.<sup>36–38</sup> Developing carbon supports with high contents of metal atoms is another available approach for the construction of dual sites, since the higher loading atoms enhance possible access to each metal atom.<sup>39–41</sup>

Covalent-organic frameworks (COFs), as crystalline polymers, are constructed with periodic arrangements of atoms in the skeletons.<sup>42–45</sup> Because of the designable skeletons and controllable pores, COFs have various applications such as for gas sorption and separation, catalysis, energy storage, and ion conduction.<sup>46–53</sup> Since 2015, COFs (COF-366-Co and COF-367-Co) have been used in CO<sub>2</sub>RR.<sup>54</sup> However, the activity and selectivity of COFs still need to be improved because of the limited conductivity of frameworks and low atomic utilization efficiency. To improve the electron conductivity along with the frameworks, COFs with fully conjugated frameworks have been developed.<sup>51</sup> To enhance the metal atomic utilization efficiency, COF sheets were synthesized using an exfoliation strategy.<sup>55</sup> Nevertheless, the limited kinds of building units result in insufficient varieties of catalytic COFs. Recently, it was found that because of the uniform and periodic distribution of different atoms, COFs could be used as precursors of functional carbons for electro/

photo-catalysis, lithium batteries, and biomass conversion.<sup>56–63</sup>

Herein, we first constructed bimetal catalysts for CO<sub>2</sub>RR with dual sites (ZnN<sub>4</sub> and CoN<sub>4</sub>O) from a core-shell hybrid of COF and a metal-organic framework (MOF). The unique core-shell framework works as an ideal template for the construction of high-density active sites. The outer COF-shell prevents the aggregation of the MOF-core and decreases the loss of Zn ions and N and O atoms in pyrolysis, which promotes the formation of high Zn active sites together with heteroatoms, and the MOF-core prevents the collapse of the COF-shell under thermal treatment. The resulting hollow carbon has a hollow structure with abundant N and O atoms (10.73% for N and 8.31% for O) on the carbon walls, which immobilizes cobalt phthalocyanine (CoPc) molecules through coordination effects. The catalysts had Co and Zn contents of 2.47 and 11.05 wt.%, respectively. The as-prepared catalyst promoted the catalysis of CO<sub>2</sub>RR with high activity and selectivity, with a maximum Faradic efficiency (FE) value for CO of 92.6% at -0.8 V.

## 2 | EXPERIMENTAL SECTION

### 2.1 | The synthesis method of COF@MOF

107.2 mg of TP in 50 mL of tetrahydrofuran (THF) and 143.9 mg of 2,2'-bipyridine-5,5'-diamine (BPY) in 50 mL of THF were added to the mixture of ZIF-8 (500 mg) and THF (250 mL), which were then sonicated for 30 min and stirred at room temperature for 24 h to obtain 2-methylimidazole zinc salt (ZIF-8)-supported TP-BPY-COF. The solid was washed with MeOH and THF in sequence and then dried in vacuum to yield COF@MOF with an isolation TP-BPY-COF yield of 75.33%.

### 2.2 | The synthesis method of COF@MOF<sub>800</sub>

The as-prepared COF@MOF (515 mg) was heated at 800°C for 1 h (5°C min<sup>-1</sup>) in N<sub>2</sub> atmosphere to yield COF@MOF<sub>800</sub> (236 mg).

### 2.3 | The synthesis method of COF@MOF<sub>800</sub>-Co

200 mg of COF@MOF<sub>800</sub> was degassed for 10 min, and then the CoPc solution (20 mg in 4 mL of THF)

was added under vacuum. The mixture was stirred for 1 h. Then, THF was removed to obtain COF@MOF<sub>800</sub>-Co.

## 2.4 | The synthesis method of COF@MOF<sub>950</sub>

The as-prepared COF@MOF (500 mg) was heated at 950°C for 1 h (5°C min<sup>-1</sup>) in N<sub>2</sub> atmosphere to yield COF@MOF<sub>950</sub> (200 mg).

## 2.5 | The synthesis method of COF@MOF<sub>950</sub>-Co

200 mg of COF@MOF<sub>950</sub> was degassed for 10 min, and then the CoPc solution (20 mg in 4 mL of THF) was added under vacuum. The mixture was stirred for 1 h. Then, THF was removed to obtain COF@MOF<sub>950</sub>-Co.

## 2.6 | CO<sub>2</sub>RR performance

Preparation of the working electrode: 5 mg of sample was ground for 10 min and dispersed in a mixed solution of 50 μL of Nafion solution (5 wt%) and ethanol (450 μL), followed by sonication for 30 min. 100 μL of as-prepared catalyst ink was directly spray-coated on a hydrophobic carbon paper (1 cm × 1 cm) to form a 1 cm<sup>2</sup> catalyst area with a catalyst loading of 1 mg cm<sup>-2</sup>. The deposited carbon paper was further dried at room temperature. All the electrochemical experiments were performed in an H-type cell with two compartments separated by an anion exchange membrane (Nafion-117). Each compartment contained 70 mL of electrolyte (0.5 M KHCO<sub>3</sub>). Electrochemical measurements were performed in a three-electrode cell using a Ag/AgCl electrode as the reference electrode and a Pt foil as the counter electrode. Before the electrochemical measurements, the electrolyte solution was purged with CO<sub>2</sub> for 30 min to obtain the CO<sub>2</sub>-saturated solution. The pH was 7.2 for CO<sub>2</sub>-saturated 0.5 M KHCO<sub>3</sub> and 8.8 for Ar-saturated 0.5 M KHCO<sub>3</sub>. A mass flow controller was used to set the Ar or CO<sub>2</sub> flow rate at 30 r.p.m. Linear sweep voltammetry (LSV) curves were constructed at a scan rate of 10 mV/s. All the potentials were reported with respect to the reversible hydrogen electrode (RHE) and calculated using the formula  $E$  (vs. RHE) =  $E$  (vs. Ag/AgCl) + 0.196 V + 0.059 × pH. Gas products were detected using gas chromatography.

## 3 | RESULTS AND DISCUSSION

The crystalline structures of the prepared ZIF-8 and COF@MOF were investigated by powder X-ray diffraction (PXRD) measurements. The PXRD patterns for ZIF-8 showed peaks at 7.42°, 10.57°, 12.93°, and 18.12°, which were from (011), (002), (112), and (222) facets (Figure 1C, blue curve), respectively, and these peaks were also identified for COF@MOF. In addition, a new peak at 3.6° was clearly identified, which was from the (100) facet of TP-BPY-COF (Figure 1C, red curve).<sup>64</sup>

Fourier infrared spectroscopy for ZIF-8 showed that the peak at 430 cm<sup>-1</sup> emerged from Zn-N bonds. Also, all the peaks from ZIF-8 were well maintained with coating of TP-BPY-COF on the surface of ZIF-8 (Figure S1). Moreover, a new bond at 1624 cm<sup>-1</sup> emerged from the imine bond of TP-BPY-COF (Figure S1, red curve), suggesting that COF was successfully synthesized.

The core-shell morphologies were revealed by scanning electron microscopy (SEM) and transmission electron microscopy (TEM) images. The SEM images showed that COF@MOF and ZIF-8 have the same dodecahedron shape and uniform particle size of 320 nm (Figure S2). Meanwhile, the TEM images showed that the outer surface of ZIF-8 became rough, and no aggregated bulks or particles were observed for COF@MOF, indicating that COF had grown uniformly on ZIF-8 (Figure S3). After thermal treatment at 800°C, the prepared COF@MOF<sub>800</sub> had a dodecahedron morphology, as revealed by SEM images and TEM images, and the cavity size was about 60 nm (Figures S4 and S5).

On absorption of CoPc in COF@MOF<sub>800</sub>, SEM images showed that the COF@MOF<sub>800</sub>-Co crystals had a dodecahedron morphology (Figure 2A), similar to that of COF@MOF<sub>800</sub>. Also, TEM images showed that the average size of COF@MOF<sub>800</sub>-Co was ~110 nm, while the average size of COF@MOF<sub>800</sub> was ~80 nm (Figure 2B and Figure S5). Additionally, TEM images indicated that COF@MOF<sub>800</sub>-Co and COF@MOF<sub>800</sub> showed well-separated nanocrystals, indicating that they were composed of amorphous carbon without metal nanoparticles and clusters. High-resolution TEM images showed that there were many vertical carbons in different directions with an inner layer distance of 0.34 nm, which emerged from the carbonization of TP-BPY-COF (Figure S6), indicating that COF@MOF<sub>800</sub>-Co and COF@MOF<sub>800</sub> were composed of standing carbon sheets. Aberration-corrected high-angle annular dark-field scanning TEM (HAADF-STEM) images for COF@MOF<sub>800</sub> showed that bright dots from the atomic dispersion of Zn were in atomic states rather than in nanoparticles dispersed on the carbon (Figure S7). With loading of CoPc, the atomic state of Zn was well retained. HAADF-STEM images for

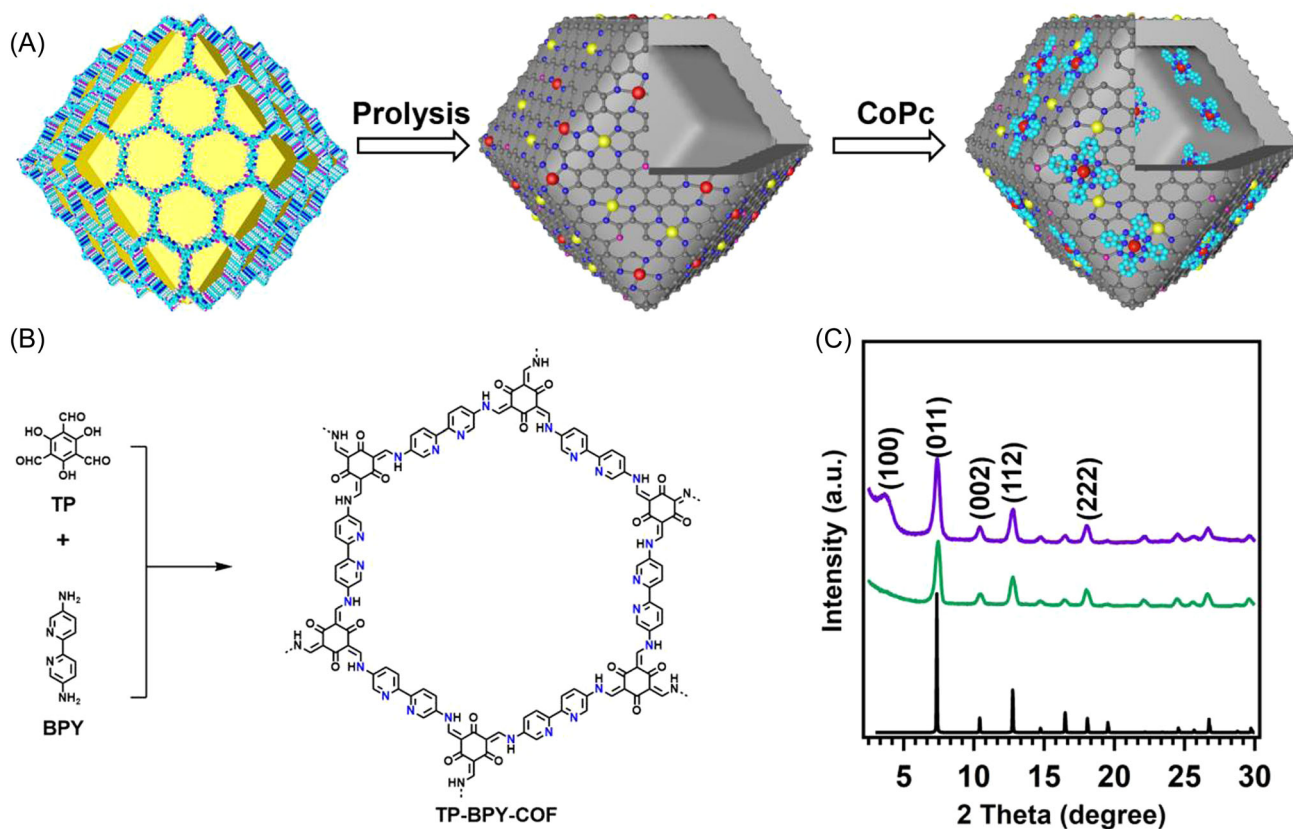


**FIGURE 1** (A) Synthesis of COF@MOF<sub>800</sub>-Co from COF@MOF. (B) Synthesis and structure of TP-BPY-COF. (C) PXRD patterns of COF@MOF (purple curve) and ZIF-8 (green curve) and simulation of ZIF-8 (black curve). COF, covalent-organic framework; MOF, metal-organic framework; PXRD, powder X-ray diffraction.

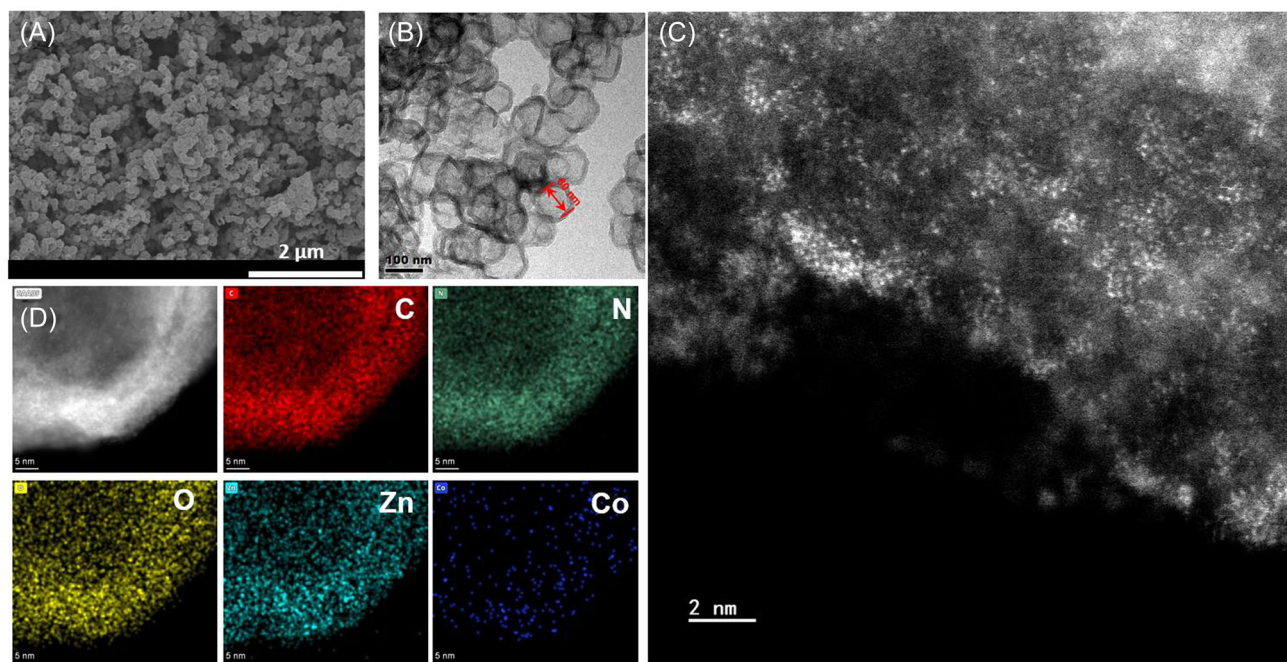


**FIGURE 2** (A) SEM image, (B) TEM image, (C) HAADF-STEM image, and (D) EDX-mapping images of COF@MOF<sub>800</sub>-Co. COF, covalent-organic framework; EDX, energy-dispersive X-ray spectroscopy; HAADF-STEM, high-angle annular dark-field scanning transmission electron microscopy; MOF, metal-organic framework; SEM, scanning electron microscopy; TEM, transmission electron microscopy.

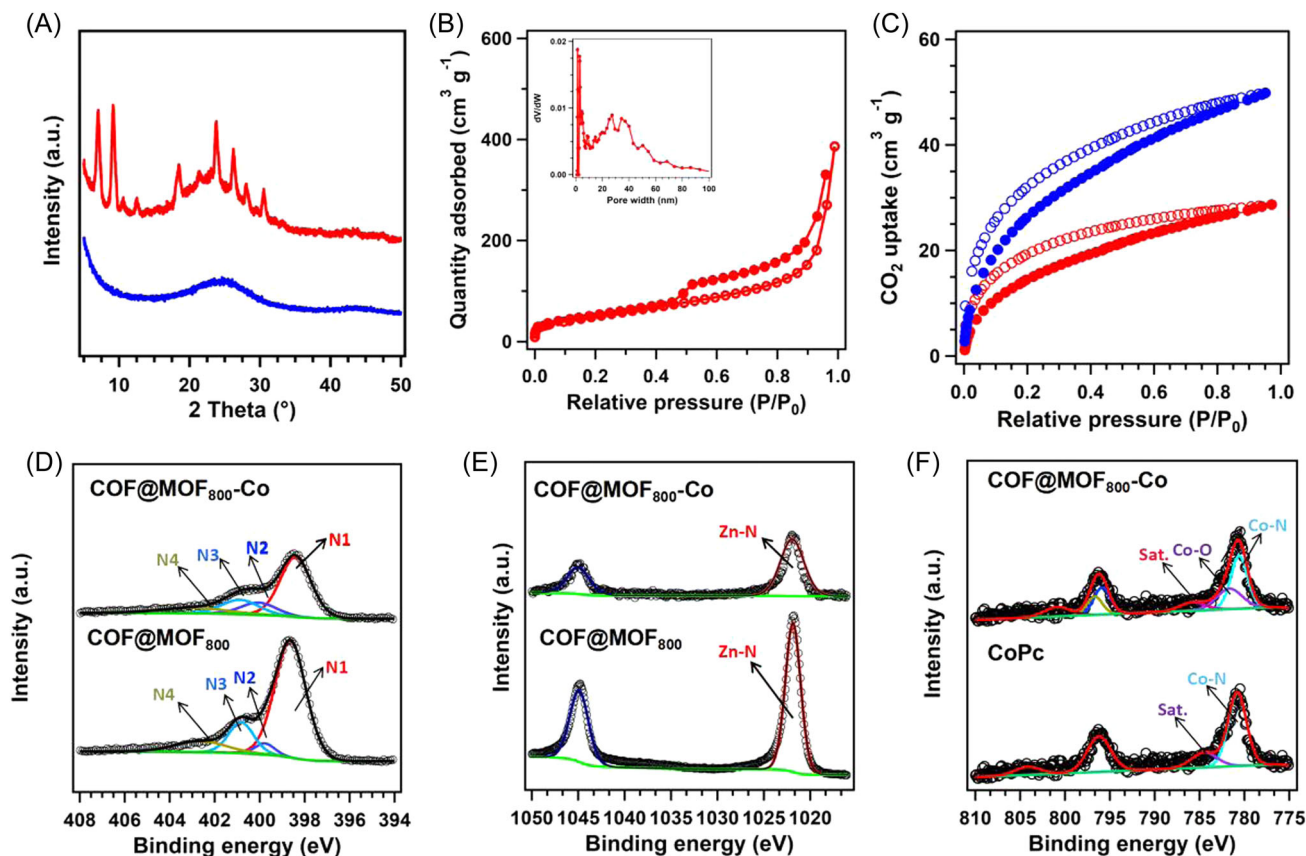


**FIGURE 3** (A) PXRD patterns of COF@MOF<sub>800</sub> (blue curve) and COF@MOF<sub>800</sub>-Co (red curve); (B) N<sub>2</sub> sorption isotherm profiles at 77 K (inset: pore size distribution curve) of COF@MOF<sub>800</sub>-Co; (C) CO<sub>2</sub> sorption curves of COF@MOF<sub>800</sub>-Co (red curve) and COF@MOF<sub>800</sub> (blue curve) at 273 K; (D) high-resolution XPS spectra of (D) N 1s and (E) Zn 2p for COF@MOF<sub>800</sub> and COF@MOF<sub>800</sub>-Co; and (F) high-resolution XPS spectra of Co 2p for COF@MOF<sub>800</sub>-Co and CoPc. COF, covalent-organic framework; CoPc, cobalt phthalocyanine; MOF, metal-organic framework; PXRD, powder X-ray diffraction; XPS, X-ray photoelectron spectroscopy.

COF@MOF<sub>800</sub>-Co showed many bright dots on the surface, which arose from atomic Zn and Co on the carbon (Figure 2C). Additionally, the energy-dispersive X-ray spectroscopy (EDX) mapping images of COF@MOF<sub>800</sub>-Co (Figure 2D) confirmed that all the elements (C, N, O, Co, and Zn) were well dispersed in the skeletons of the carbon.

The PXRD patterns of COF@MOF<sub>800</sub> demonstrated that the peaks at 24.8° and 42.2° arose from the (002) and (101) facets of carbon (Figure 3A, blue curve). Also, many peaks were observed in COF@MOF<sub>800</sub>-Co (Figure 3A, red curve), which arose from CoPc. Moreover, peaks from (002) and (101) of carbon were also observed (Figure 3A, red curve). Notably, there were no characteristic peaks for metal nanoparticles or oxides, indicating that there were no large particles or clusters, which was consistent with the results revealed by SEM and TEM images as mentioned above.

The N<sub>2</sub> sorption curves of COF@MOF<sub>800</sub>-Co and COF@MOF<sub>800</sub> showed type-IV isotherms, indicating that the N<sub>2</sub> sorption was mainly contributed by the mesopore

and macropore structures (Figure 3B and Figure S9). The Brunauer-Emmett-Teller surface area for COF@MOF<sub>800</sub> was 292.06 m<sup>2</sup> g<sup>-1</sup>, with a pore volume of 0.95 cm<sup>3</sup> g<sup>-1</sup>, while the COF@MOF<sub>800</sub>-Co had a decreased surface area of 182.46 m<sup>2</sup> g<sup>-1</sup> and a pore volume of 0.60 cm<sup>3</sup> g<sup>-1</sup>. The pore size distribution curves showed that the pores ranged in size from 20 to 60 nm, while the pore sizes of COF@MOF<sub>800</sub>-Co had a wide range from 0.5 to 60 nm, demonstrating that there were micro-/meso-/macroporous hierarchical channels in COF@MOF<sub>800</sub>-Co (Figure 3B, inset).

We then investigated the CO<sub>2</sub> sorption behavior at 273 K. The CO<sub>2</sub> sorption curves revealed that COF@MOF<sub>800</sub> has a higher CO<sub>2</sub> capacity of 49.85 cm<sup>3</sup> g<sup>-1</sup> (Figure 3C, blue curve) than that of COF@MOF<sub>800</sub>-Co (28.69 cm<sup>3</sup> g<sup>-1</sup>) (Figure 3C, red curve). The high CO<sub>2</sub> uptakes for COF@MOF<sub>800</sub> contributed to abundant O and N sites on the surface of the carbon. With binding of CoPc, the binding sites were occupied by CoPc, which resulted in lower surface areas and a lower CO<sub>2</sub> uptake.

Raman spectra of COF@MOF<sub>800</sub>-Co and COF@MOF<sub>800</sub> showed two peaks at 1350 and 1587 cm<sup>-1</sup>, corresponding to the D and G bands of sp<sup>2</sup> carbon, respectively. The intensity ratios of the D and G bands ( $I_D/I_G$ ) indicated disorders and defects in the carbon. The  $I_D/I_G$  values for COF@MOF<sub>800</sub>-Co and COF@MOF<sub>800</sub> were about 0.94 (Figure S9, red curve) and 0.92 (Figure S9, blue curve), respectively, suggesting that their graphitization degrees were well retained after binding CoPc.

To determine the chemical states of COF@MOF<sub>800</sub>-Co and COF@MOF<sub>800</sub>, X-ray photoelectron spectroscopy (XPS) was performed. The XPS spectra for COF@MOF<sub>800</sub>-Co and COF@MOF<sub>800</sub> showed peaks from C 1s, N 1s, O 1s, and Zn 2p (Figure S10A). The contents of Zn, N, and O in COF@MOF<sub>800</sub> were 10.54, 9.19, and 7.87 wt.%, respectively. We prepared ZIF<sub>800</sub> under the same conditions to prove the shell effects of the COF. Specifically, the XPS spectra of ZIF<sub>800</sub> showed that the contents of Zn, N, O, and Zn were 8.31, 7.56, and 6.33 wt.%, respectively (Figure S10B), which were lower than those in COF@MOF<sub>800</sub>, which confirmed that the COF-shell prevents the loss of Zn ions, N atoms, and O atoms. With absorption of CoPc, the contents for Zn, N, O, and Co were 12.05, 15.73, 8.31, and 2.53 wt.%, respectively. The high-resolution N 1s spectrum of COF@MOF<sub>800</sub> can be deconvoluted into four distinct peaks of pyridinic N (N1), pyrrolic N (N2), graphite N (N3), and quaternary N (N4) at 398.48, 399.86, 400.82, and 402.92 eV, with corresponding relative contents of 68.69%, 6.58%, 18.18%, and 6.54%, respectively. The corresponding contents of N1, N2, N3, and N4 for COF@MOF<sub>800</sub>-Co were 64.89%, 13.27%, 15.63%, and 6.21%, respectively (Figure 3D). The high-resolution Zn 2p spectra of COF@MOF<sub>800</sub>-Co and COF@MOF<sub>800</sub> showed two distinct peaks at 1021.85 eV (2p<sub>3/2</sub>) and 1044.89 eV (2p<sub>1/2</sub>), attributed to Zn-N bonds (Figure 3E). Additionally, the Co 2p spectra of COF@MOF<sub>800</sub>-Co can be deconvoluted into peaks of Co 2p<sub>1/2</sub> and Co 2p<sub>3/2</sub>, with the corresponding satellite peaks at around 800.84 and 785.78 eV, respectively. The peak at 780.58 eV was attributed to Co-N and another new peak at 781.66 eV was attributed to Co-O, in which the relative contents for Co-N and Co-O were 46.71 and 12.73 %, respectively. In addition, there was no Co-O peak at the Co 2p spectra of CoPc (Figure 3F).

To further confirm the electronic and atomic states of Co and Zn in COF@MOF<sub>800</sub> and COF@MOF<sub>800</sub>-Co, X-ray absorption fine structure (XAFS) analysis was performed. The locations of the Zn absorption near edge of COF@MOF<sub>800</sub> (Figure 4A, blue curve) and COF@MOF<sub>800</sub>-Co (Figure 4A, red curve) showed different structures from the Zn foil (Figure 4A, black curve) and

ZnO (Figure 4A, yellow curve), but the location of the Zn absorption in COF@MOF<sub>800</sub> was close to that of ZnPc (Figure 4A, black curve). Furthermore, the peak position of Zn in the R-space of COF@MOF<sub>800</sub> and COF@MOF<sub>800</sub>-Co was 1.98 Å, which was close to that of the ZnPc coordination (Figure 4B). In addition, the extended X-ray absorption fine structure (EXAFS) fitting results confirmed that Zn atoms in COF@MOF<sub>800</sub> and COF@MOF<sub>800</sub>-Co were coordinated by Zn-N<sub>4</sub> (Figure S11). Correspondingly, the Co K-edge X-ray absorption near edge structure spectra of COF@MOF<sub>800</sub>-Co (Figure 4C, yellow curve) showed that the position of the near-edge absorption was different from those of CoPc (Figure 4C, blue curve) and the Co foil (Figure 4C, black curve). Moreover, the position of Co in COF@MOF<sub>800</sub>-Co in the R-space showed that it has similar Co-N and Co-O coordinations, with peaks at about 1.90 and 2.07 Å, respectively (Figure 4D). Furthermore, the EXAFS fitting results of COF@MOF<sub>800</sub>-Co revealed that Co was present in the CoN<sub>4</sub>O coordinated model (Figure S12 and Table S1). Thus, Co and Zn existed as CoN<sub>4</sub>O and ZnN<sub>4</sub> in COF@MOF<sub>800</sub>-Co, respectively. Additionally, to further confirm the combination of Co, wavelet transform of the Co L3-edge EXAFS oscillations was conducted (Figure 5E). COF@MOF<sub>800</sub>-Co and CoPc showed an intensity maximum at 2.2 Å<sup>-1</sup> (Co-N). In contrast, for the Co foil, only a predominant intensity maximum at a higher k-space (6.5 Å<sup>-1</sup>) was detected, suggesting the absence of Co-Co metallic coordination. This further confirmed that no metal nanoparticles are present in COF@MOF<sub>800</sub>-Co.

Given the high densities of CoN<sub>4</sub>O and ZnN<sub>4</sub> in COF@MOF<sub>800</sub>-Co, we have investigated the catalytic performance of CO<sub>2</sub>RR for COF@MOF<sub>800</sub>-Co in 0.5 M KHCO<sub>3</sub> using the H-type cell, which is separated by a proton-exchange membrane. As a control, the electrocatalytic performance of COF@MOF<sub>800</sub> was also investigated. LSV for COF@MOF<sub>800</sub>-Co and COF@MOF<sub>800</sub> was conducted from 0 to -1.0 V (vs. RHE) at a scan rate of 10 mV s<sup>-1</sup> under a CO<sub>2</sub> or Ar atmosphere, respectively. The LSV curves for COF@MOF<sub>800</sub>-Co (red curve) and COF@MOF<sub>800</sub> (blue curve) showed that the current densities under the CO<sub>2</sub> atmosphere (solid curve) were much higher than those under the Ar atmosphere (dotted line) at the same potentials, indicating that their activities originated from CO<sub>2</sub>RR (Figure 5A). The onset potential ( $E_o$ ) determined at a current density of 1 mA cm<sup>-2</sup> for COF@MOF<sub>800</sub>-Co was 0.38 V, which was more positive than that of COF@MOF<sub>800</sub> (0.53 V) in CO<sub>2</sub>, suggesting that the activity of COF@MOF<sub>800</sub>-Co is higher than that of COF@MOF<sub>800</sub>. The Tafel slope is a significant parameter to elucidate the rate-determining step (RDS) of CO<sub>2</sub>RR. The corresponding Tafel slope of

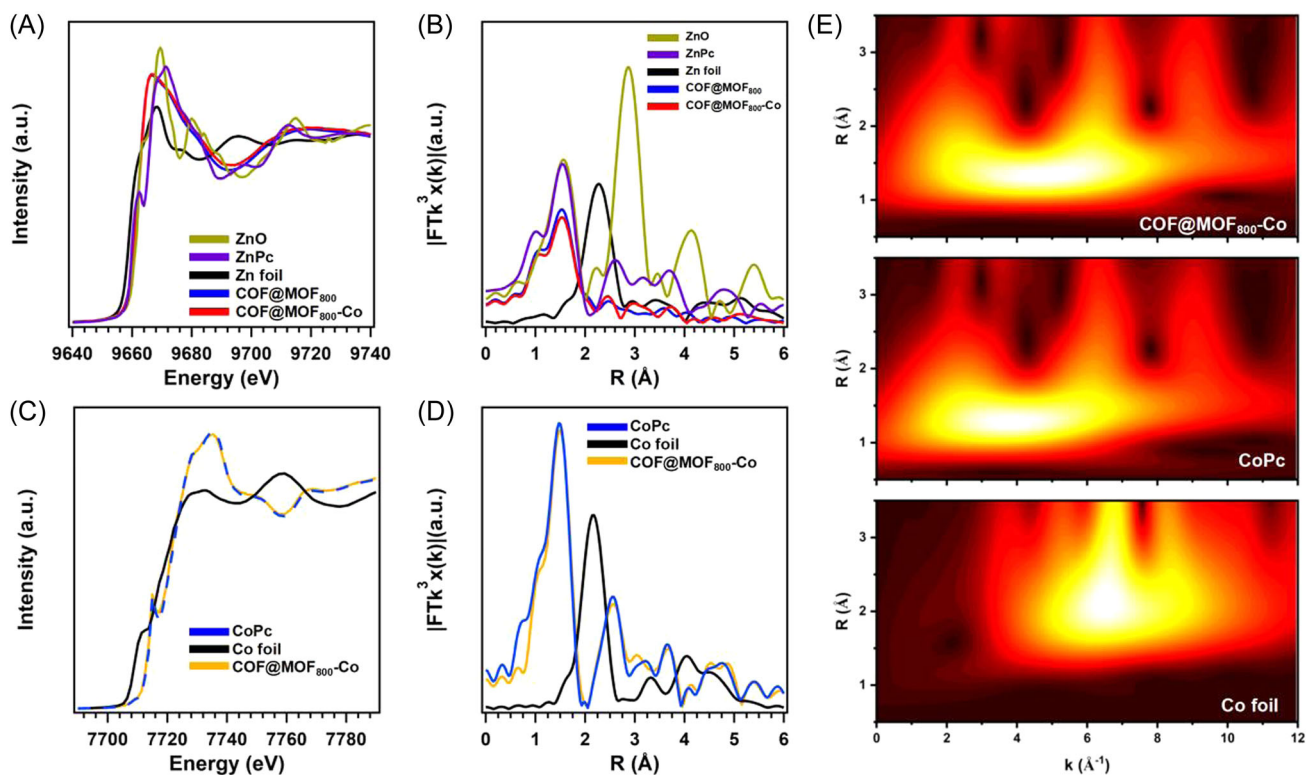


**FIGURE 4** (A) XANES spectra and (B) K-edge  $k^3$ -weighted Fourier transform spectra from EXAFS for Zn of the Zn foil (black curve) ZnO (yellow curve), ZnPc (purple curve), COF@MOF<sub>800</sub> (blue curve), and COF@MOF<sub>800</sub>-Co (red curve). (C) XANES spectra and (D) K-edge  $k^3$ -weighted Fourier transform spectra for Co spectra from EXAFS of CoPc (blue curve), a Co foil (black curve), and COF@MOF<sub>800</sub>-Co (yellow curve). (E) WT-EXAFS of the a Co foil, CoPc, and COF@MOF<sub>800</sub>-Co. COF, covalent-organic framework; CoPc, cobalt phthalocyanine; EXAFS, extended X-ray absorption fine structure; MOF, metal-organic framework; WT, wavelet transform; XANES, X-ray absorption near edge structure.

COF@MOF<sub>800</sub>-Co (Figure 5B, red curve) was 350 mV dec<sup>-1</sup>, smaller than that of COF@MOF<sub>800</sub> (492 mV dec<sup>-1</sup>) (Figure 5B, blue curve), indicating its better kinetic behavior.<sup>29</sup> The gas chromatography-mass spectrometry measurement showed that only CO and H<sub>2</sub> were produced, without the formation of any other products during the process of CO<sub>2</sub>RR. The Faradic efficiencies of CO (FE<sub>CO</sub>) were determined for the catalysts at different potentials. COF@MOF<sub>800</sub>-Co had FE<sub>CO</sub> values of 69.9%, 83.1%, 89.2%, 92.6%, 92.4%, and 89.1% at -0.5, -0.6, -0.7, -0.8, -0.9, and -1.0 V (Figure 4C, red curve), respectively. Also, the maximum FE<sub>CO</sub> reached 92.6% at -0.8 V, which was higher than those of many other single and dual atomic electrocatalysts (Table S2).<sup>65,66</sup> On the contrary, COF@MOF<sub>800</sub> showed low activity and selectivity toward CO<sub>2</sub>RR, with FE<sub>CO</sub> values of 16.19%, 13.06%, 14.07%, 13.95%, 14.51%, and 14.82%, respectively, in the same potential ranges (Figure 5C, blue curve). To confirm the suppressed effects on HER, we have calculated the FE of H<sub>2</sub> (FE<sub>H<sub>2</sub></sub>) for the catalysts. Accordingly, without the CoN<sub>4</sub>O site in the catalysts, COF@MOF<sub>800</sub> had a much higher activity for HER, with

FE<sub>H<sub>2</sub></sub> values of 83.81%, 86.94%, 85.93%, 86.05%, 85.49%, and 85.18% at -0.5, -0.6, -0.7, -0.8, -0.9, and -1.0 V, respectively (Figure S13, blue curve). Also, the corresponding FE<sub>H<sub>2</sub></sub> values for COF@MOF<sub>800</sub>-Co were 30.1%, 16.9%, 10.8%, 7.4%, 7.6%, and 19.9% at -0.5, -0.6, -0.7, -0.8, -0.9, and -1.0 V, respectively (Figure S13, red curve). Thus, the HER was successfully suppressed.

Meanwhile, we prepared COF@MOF<sub>950</sub>-Co containing CoN<sub>4</sub>O sites without ZnN<sub>4</sub> sites and investigated the CO<sub>2</sub>RR activity. COF@MOF<sub>950</sub>-Co had an E<sub>o</sub> value of 0.46 V, which was more negative than that of COF@MOF<sub>800</sub>-Co. Also, the corresponding values of FE<sub>CO</sub> for COF@MOF<sub>950</sub>-Co were 45.5%, 62.4%, 74.2%, 76.7%, 67.5%, and 44.8% at -0.5, -0.6, -0.7, -0.8, -0.9, and -1.0 V, respectively (Figures S14A and S14B). This suggested that the synergistic effects of CoN<sub>4</sub>O and ZnN<sub>4</sub> in COF@MOF<sub>800</sub>-Co led to higher CO<sub>2</sub>RR performance than that of solely the CoN<sub>4</sub>O site in COF@MOF<sub>950</sub>-Co or the ZnN<sub>4</sub> site in COF@MOF<sub>800</sub>. The partial current densities ( $j_{CO}$ ) of COF@MOF<sub>800</sub>-Co (Figure 5D, red curve) increased with increasing potential, yielding 15.57 mA cm<sup>-2</sup> at -1.0 V, which is

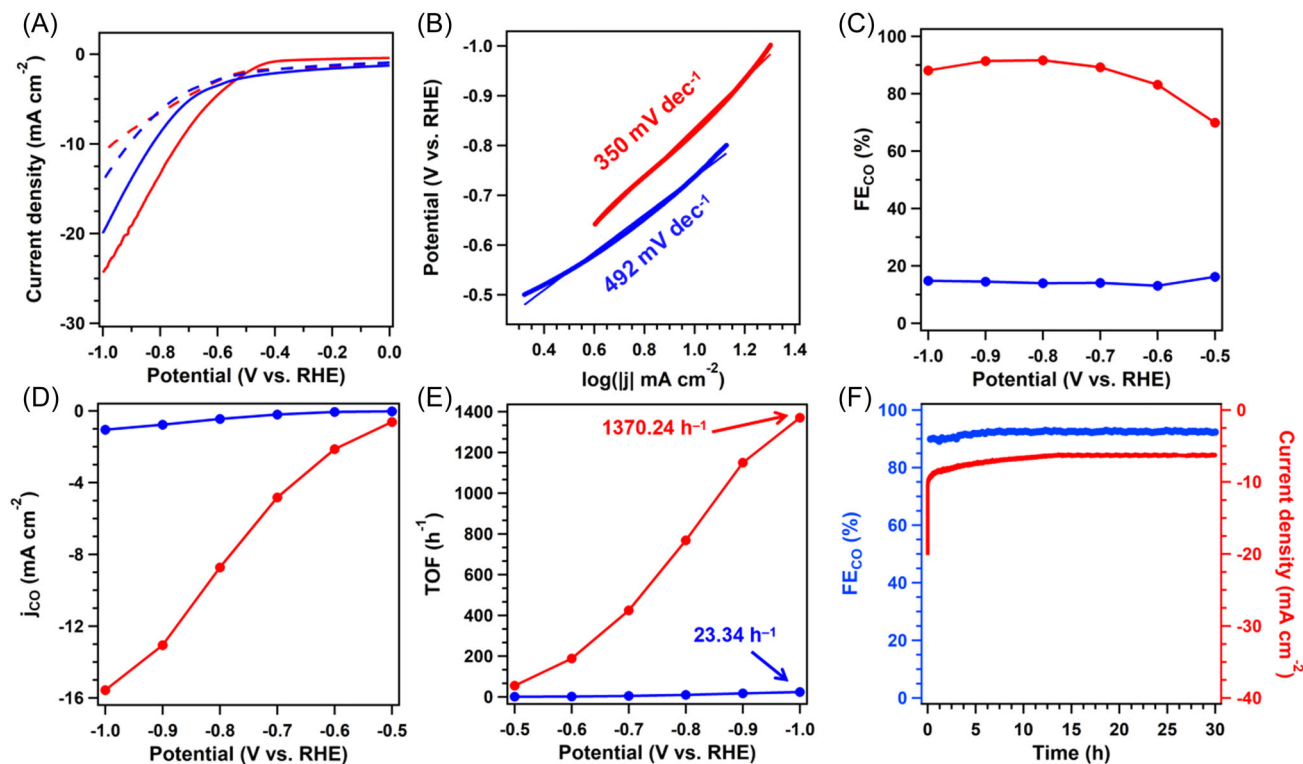


**FIGURE 5** (A) LSV curve in CO<sub>2</sub> (solid line) and Ar atmosphere (dotted line) at a scan rate of 10 mV s<sup>-1</sup>; (B) the corresponding Tafel slope; (C) FE<sub>CO</sub> calculated from -0.5 to -1.0 V; (D) partial CO current density; and (E) corresponding TOF values at different applied potentials for COF@MOF<sub>800</sub>-Co (red curve) and COF@MOF<sub>800</sub> (blue curve). (F) Current density (red curve) and FE<sub>CO</sub> (blue curve) for COF@MOF<sub>800</sub>-Co measured at 0.85 V versus RHE for 30 h. FE<sub>CO</sub>, Faradic efficiencies of CO; LSV, linear sweep voltammetry; RHE, reversible hydrogen electrode.

significantly higher than that of COF@MOF<sub>800</sub> (1.05 mA cm<sup>-2</sup>) (Figure 5D). Furthermore, the turnover frequency (TOF) values of COF@MOF<sub>800</sub>-Co (Figure 5E, red curve) and COF@MOF<sub>800</sub> (Figure 5E, blue curve) were calculated from -0.5 to -1.0 V. The TOF value of COF@MOF<sub>800</sub>-Co reached the highest value of 1370.24 h<sup>-1</sup> at -1.0 V, while the highest TOF value for COF@MOF<sub>800</sub> was 23.34 h<sup>-1</sup> at -1.0 V. Thus, COF@MOF<sub>800</sub>-Co showed much higher activity and selectivity than COF@MOF<sub>800</sub>.

Electrochemical impedance spectroscopy was conducted to investigate the different ionic and electronic transport behaviors of COF@MOF<sub>800</sub>-Co and COF@MOF<sub>800</sub>. According to the Nyquist plots, COF@MOF<sub>800</sub>-Co has a lower transfer resistance ( $R_{ct}$ ) of 95.1  $\Omega$  (Figure S15, red curve) than COF@MOF<sub>800</sub> (99.3  $\Omega$ ) (Figure S15, blue curve), indicating that there was a fast electron-transfer process of CO<sub>2</sub>RR on the surface of COF@MOF<sub>800</sub>-Co. This suggested that the synergy of CoN<sub>4</sub>O and ZnN<sub>4</sub> can facilitate electron transport.

The electrochemical active surface area (ECSA) can provide the capacitance to evaluate the performance of electrocatalysts (Figure S15). Accordingly, COF@MOF<sub>800</sub>-Co (red curve) had a smaller ECSA of 9.1 mF cm<sup>-2</sup> than COF@MOF<sub>800</sub> (29.7 mF cm<sup>-2</sup>, blue curve). The low ECSA

was due to the inner and outer surfaces of the carbon shell of COF@MOF<sub>800</sub> being covered by CoPc (Figure 5E).

The long-term stability is a major issue for SACs toward CO<sub>2</sub>RR. The durable stability of COF@MOF<sub>800</sub>-Co was investigated at -0.8 V for 30 h. The current density was 10 mA cm<sup>-2</sup> after 30 h (Figure 5F, red curve), which is about 94.5% of the initial value, and FE<sub>CO</sub> was well retained (92.6%) (Figure 5F, blue curve).

To investigate the catalytic performance of COF@MOF<sub>800</sub>-Co for CO<sub>2</sub>RR, we carried out a DFT calculation to determine the lowest Gibbs free energy pathway for CO<sub>2</sub>RR on Co sites (Figure 6A) and Zn sites (Figure 6B) in COF@MOF<sub>800</sub>-Co and Zn sites (Figure 6C) in COF@MOF<sub>800</sub>. The CO<sub>2</sub>RR mainly involved three steps: CO<sub>2</sub> was absorbed and protonated to form \*COOH, which was then converted into \*CO; finally, \*CO dissociated from the metal sites to form CO molecular and desorbed. Accordingly, the RDS for the three models is the generation of COOH\*. The free-energy change ( $\Delta G$ ) for Co sites in COF@MOF<sub>800</sub>-Co was 0.25 eV, much lower than those of Zn sites of COF@MOF<sub>800</sub>-Co (0.58 eV) and COF@MOF<sub>800</sub> (1.32 eV) (Figure 6D). Considering that HER is the competing reaction for CO<sub>2</sub>RR, the corresponding  $\Delta G$ s for HER on three different sites

were calculated. The RDS for Co sites was from  $H^*$  to  $H_2$  with  $\Delta G$ , while the RDS for the Zn sites in COF@MOF<sub>800</sub>-Co (0.58 eV) and COF@MOF<sub>800</sub> was the formation of the  $H^*$  on the catalytic sites, with  $\Delta G$  of 0.36 eV and 0.70 eV for ZnN<sub>4</sub>-O, respectively (Figure 6E), suggesting that the Co sites had higher activity for HER than Zn sites. To clearly identify the catalytic process, the limiting potential differences between CO<sub>2</sub>RR and HER (UL(CO<sub>2</sub>)-UL(H<sub>2</sub>)) were also calculated. UL(CO<sub>2</sub>)-UL(H<sub>2</sub>) for Co sites was -0.11 eV, indicating that the HER was successfully suppressed by CO<sub>2</sub>RR. Different from Co sites, the main reactions for Zn sites were HER, and the UL(CO<sub>2</sub>)-UL(H<sub>2</sub>) for Zn sites in COF@MOF<sub>800</sub>-Co and COF@MOF<sub>800</sub> were 0.21 and 0.62 eV, respectively. The smaller value of UL(CO<sub>2</sub>)-UL(H<sub>2</sub>) indicates that the

synergistic effects of Co and Zn in COF@MOF<sub>800</sub>-Co promoted suppression of the competing reaction (HER).

## 4 | CONCLUSION

In summary, we have developed a new synergetic dual atomic catalyst for CO<sub>2</sub>RR. The synergistic CoN<sub>4</sub>O and ZnN<sub>4</sub> sites significantly improve the electron transport rate and the generation of a COOH\* intermediate, which is beneficial to the process of CO<sub>2</sub>RR. The catalyst showed superior activity selectivity and long-term stability over many other electrocatalysts. Its maximum FE<sub>CO</sub> and TOF values reached 92.6% at -0.8 V and 1370.24 h<sup>-1</sup> at -1.0 V. This work not only provides new

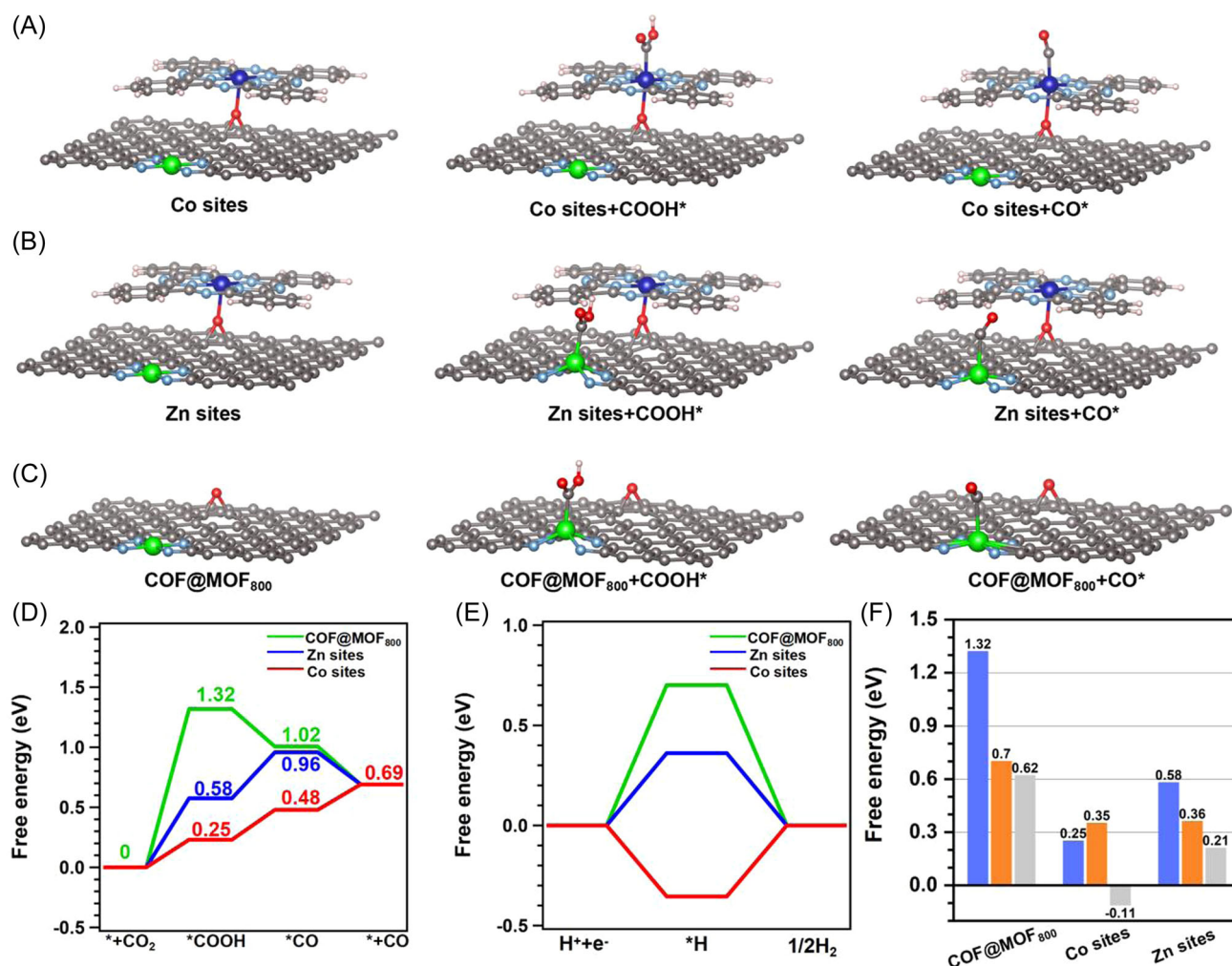


FIGURE 6 Schematic mechanism for CO<sub>2</sub>RR on (A) Co sites and (B) Zn sites in COF@MOF<sub>800</sub>-Co, and (C) Zn sites in COF@MOF<sub>800</sub>. The balls in green, blue, gray, cyan, red, and pink represent Zn, Co, C, N, O, and H atoms, respectively. (D) Relative energy diagram of CO<sub>2</sub>RR and (E) HER for Co sites (red curve) and Zn sites (green curve) in COF@MOF<sub>800</sub>-Co and (C) Zn sites (blue curve) in COF@MOF<sub>800</sub> (blue curve). (F) Overpotentials for the rate-determining steps of the catalytic sites in CO<sub>2</sub>RR (blue: CO<sub>2</sub>RR; orange: HER; gray: the values of UL(CO<sub>2</sub>)-UL(H<sub>2</sub>)). CO<sub>2</sub>RR, carbon dioxide reduction reaction; COF, covalent-organic framework; HER, hydrogen evolution reaction; MOF, metal-organic framework.

insights for the preparation of carbon-supported bimetallic SACs but also presents a new method to develop catalytic carbons from COFs.

## ACKNOWLEDGMENTS

Q. Xu acknowledges financial support from the Natural Science Foundation of Shanghai (20ZR1464000). G. Zeng is grateful for the support from the National Natural Science Foundation of China (21878322, 22075309) and the Science and Technology Commission of Shanghai (19ZR1479200). The authors also thank the Shanghai Synchrotron Radiation Facility for XAFS measurements at Beamline BL14w1.

## CONFLICTS OF INTEREST

The authors declare no conflicts of interest.

## ORCID

Qing Xu  <http://orcid.org/0000-0002-9066-9837>

## REFERENCES

- Nitopi S, Bertheussen E, Scott SB, et al. Progress and perspectives of electrochemical CO<sub>2</sub> Reduction on copper in aqueous electrolyte. *Chem Rev.* 2019;119(12):7610-7672.
- Wang L, Chen W, Zhang D, et al. Surface strategies for catalytic CO<sub>2</sub> reduction: from two-dimensional materials to nanoclusters to single atoms. *Chem Soc Rev.* 2019;48(21):5310-5349.
- Yang D, Zuo S, Yang H, Zhou Y, Lu Q, Wang X. Tailoring layer number of 2D porphyrin-based MOFs towards photo-coupled electroreduction of CO<sub>2</sub>. *Adv Mater.* 2022;34(7):2107293.
- Zeng Z, Gan LY, Bin Yang H, et al. Orbital coupling of hetero-diatom nickel-iron site for bifunctional electrocatalysis of CO<sub>2</sub> reduction and oxygen evolution. *Nat Commun.* 2021;12:4088.
- Zhang Y, Dong LZ, Li S, et al. Coordination environment dependent selectivity of single-site-Cu enriched crystalline porous catalysts in CO<sub>2</sub> reduction to CH<sub>4</sub>. *Nat Commun.* 2021;12:6390.
- Zheng Y, Vasileff A, Zhou X, Jiao Y, Jaroniec M, Qiao Z. Understanding the roadmap for electrochemical reduction of CO<sub>2</sub> to multi-carbon oxygenates and hydrocarbons on copper-based catalysts. *J Am Chem Soc.* 2019;141(19):7646-7659.
- Zhu Q, Murphy J, Baker R. Opportunities for electrocatalytic CO<sub>2</sub> reduction enabled by surface ligands. *J Am Chem Soc.* 2022;144(7):2829-2840.
- Liu J, Yang D, Zhou Y, et al. Tricycloquinazoline-based 2D conductive metal-organic frameworks as promising electrocatalysts for CO<sub>2</sub> reduction. *Angew Chem Int Ed.* 2021;60(26):14473-14479.
- Majidi L, Ahmadiparidari A, Shan N, et al. 2D copper tetrahydroquinone conductive metal-organic framework for selective CO<sub>2</sub> electrocatalysis at low overpotentials. *Adv Mater.* 2021;33(10):2004393.
- Mariano RG, Kang M, Wahab OJ, et al. Microstructural origin of locally enhanced CO<sub>2</sub> electroreduction activity on gold. *Nat Mater.* 2021;20(7):1000-1006.
- Zhu S, Delmo EP, Li T, et al. Recent advances in catalyst structure and composition engineering strategies for regulating CO<sub>2</sub> electrochemical reduction. *Adv Mater.* 2021;33(50):2005484.
- Geng B, Yan F, Zhang X, et al. Conductive CuCo-based bimetal organic framework for efficient hydrogen evolution. *Adv Mater.* 2021;33(49):2106781.
- Kibria MG, Edwards JP, Gabardo CM, et al. Electrochemical CO<sub>2</sub> reduction into chemical feedstocks: from mechanistic electrocatalysis models to system design. *Adv Mater.* 2019;31(31):1807166.
- Kim D, Yu S, Zheng F, et al. Selective CO<sub>2</sub> electrocatalysis at the pseudocapacitive nanoparticle/ordered-ligand interlayer. *Nat Energy.* 2020;5(12):1032-1042.
- Limaye M, Zeng S, Willard P, Manthiram K. Bayesian data analysis reveals no preference for cardinal Tafel slopes in CO<sub>2</sub> reduction electrocatalysis. *Nat Commun.* 2021;12:703.
- Cheng Y, Zhao S, Johannessen B, et al. Atomically dispersed transition metals on carbon nanotubes with ultrahigh loading for selective electrochemical carbon dioxide reduction. *Adv Mater.* 2018;30(13):1706287.
- Jeoung H, Dobbek H. Carbon dioxide activation at the Ni,Fe-cluster of anaerobic carbon monoxide dehydrogenase. *Science.* 2007;318(5855):1461-1464.
- Yan L, Xie L, Wu XL, et al. Precise regulation of pyrrole-type single-atom Mn-N<sub>4</sub> sites for superior pH-universal oxygen reduction. *Carbon Energy.* 2021;3(6):856-865.
- Cai Y, Fu J, Zhou Y, et al. Insights on forming N,O-coordinated Cu single-atom catalysts for electrochemical reduction CO<sub>2</sub> to methane. *Nat Commun.* 2021;12:586.
- Chang J, Wang G, Wang M, et al. Improving Pd-N-C fuel cell electrocatalysts through fluorination-driven rearrangements of local coordination environment. *Nat Energy.* 2021;6(12):1144-1153.
- Di J, Chen C, Yang SZ, et al. Isolated single atom cobalt in Bi<sub>3</sub>O<sub>4</sub>Br atomic layers to trigger efficient CO<sub>2</sub> photoreduction. *Nat Commun.* 2019;10:2840.
- Guo J, Zhang W, Zhang LH, et al. Control over electrochemical CO<sub>2</sub> reduction selectivity by coordination engineering of tin single-atom catalysts. *Adv Sci.* 2021;8(23):2102884.
- Jiang Z, Wang T, Pei J, et al. Discovery of main group single Sb-N<sub>4</sub> active sites for CO<sub>2</sub> electroreduction to formate with high efficiency. *Energy Environ Sci.* 2020;13(9):2856-2863.
- Jiao J, Lin R, Liu S, et al. Copper atom-pair catalyst anchored on alloy nanowires for selective and efficient electrochemical reduction of CO<sub>2</sub>. *Nat Chem.* 2019;11(3):222-228.
- Ju L, Tan X, Mao X, et al. Controllable CO<sub>2</sub> electrocatalytic reduction via ferroelectric switching on single atom anchored In<sub>2</sub>Se<sub>3</sub> monolayer. *Nat Commun.* 2021;12:5128.
- Nguyen DLT, Kim Y, Hwang YJ, Won DH. Progress in development of electrocatalyst for CO<sub>2</sub> conversion to selective CO production. *Carbon Energy.* 2020;2(1):72-98.
- Vijay S, Ju W, Brückner S, Tsang C, Strasser P, Chan K. Unified mechanistic understanding of CO<sub>2</sub> reduction to CO on transition metal and single atom catalysts. *Nat Catal.* 2021;4(12):1024-1031.

28. Birdja Y, Pérez-Gallent E, Figueiredo C, Göttle J, Calle-Vallejo F, Koper M. Advances and challenges in understanding the electrocatalytic conversion of carbon dioxide to fuels. *Nat Energy*. 2019;4(9):732-745.
29. Burdyny T, Smith W. CO<sub>2</sub> reduction on gas-diffusion electrodes and why catalytic performance must be assessed at commercially-relevant conditions. *Energy Environ Sci*. 2019;12(5):1442-1453.
30. Cobb SJ, Badiani VM, Dharani AM, et al. Fast CO<sub>2</sub> hydration kinetics impair heterogeneous but improve enzymatic CO<sub>2</sub> reduction catalysis. *Nat Chem*. 2022;14(4):417-422.
31. Gao D, Arán-Ais M, Jeon S, Roldan B. Rational catalyst and electrolyte design for CO<sub>2</sub> electroreduction towards multi-carbon products. *Nat Catal*. 2019;2(3):198-210.
32. Lin L, Li H, Wang Y, et al. Temperature-dependent CO<sub>2</sub> electroreduction over Fe-N-C and Ni-N-C single-atom catalysts. *Angew Chem Int Ed*. 2021;60(51):26582-26586.
33. Fu J, Dong J, Si R, et al. Synergistic effects for enhanced catalysis in a dual single-atom catalyst. *ACS Catal*. 2021;11(4):1952-1961.
34. Zhang L, Si R, Liu H, et al. Atomic layer deposited Pt-Ru dual-metal dimers and identifying their active sites for hydrogen evolution reaction. *Nat Commun*. 2019;10:4936.
35. Zheng T, Liu C, Guo C, et al. Copper-catalysed exclusive CO<sub>2</sub> to pure formic acid conversion via single-atom alloying. *Nat Nanotechnol*. 2021;16(12):1386-1393.
36. Chen H, Zhang Y, He Q, et al. A facile route to fabricate double atom catalysts with controllable atomic spacing for the r-WGS reaction. *J Mater Chem A*. 2020;8(5):2364-2368.
37. Chen J, Li H, Fan C, et al. Dual single-atomic Ni-N<sub>4</sub> and Fe-N<sub>4</sub> sites constructing Janus hollow graphene for selective oxygen electrocatalysis. *Adv Mater*. 2020;32(30):2003134.
38. Wei YS, Sun L, Wang M, et al. Fabricating dual-atom iron catalysts for efficient oxygen evolution reaction: a heteroatom modulator approach. *Angew Chem Int Ed*. 2020;59(37):16013-16022.
39. Guo L, Sun J, Wei J, Liu Y, Hou L, Yuan C. Conductive metal-organic frameworks: recent advances in electrochemical energy-related applications and perspectives. *Carbon Energy*. 2020;2(2):203-222.
40. Xu Q, Li Q, Guo Y, et al. Multiscale hierarchically engineered carbon nanosheets derived from covalent organic framework for potassium-ion batteries. *Small Methods*. 2020;4(9):2000159.
41. Zhou W, Su H, Li Y, et al. Identification of the evolving dynamics of coordination-unsaturated iron atomic active sites under reaction conditions. *ACS Energy Lett*. 2021;6(9):3359-3366.
42. Côté AP, Benin AI, Ockwig NW, O'Keeffe M, Matzger AJ, Yaghi OM. Porous, crystalline, covalent organic frameworks. *Science*. 2005;310(5751):1166-1170.
43. Feng X, Ding X, Jiang D. Covalent organic frameworks. *Chem Soc Rev*. 2012;41(18):6010-6022.
44. Xu H, Gao J, Jiang D. Stable, crystalline, porous, covalent organic frameworks as a platform for chiral organocatalysts. *Nat Chem*. 2015;7(11):905-912.
45. Huang N, Lee KH, Yue Y, et al. A Stable and conductive metallophthalocyanine framework for electrocatalytic carbon dioxide reduction in water. *Angew Chem Int Ed*. 2020;59(38):16587-16593.
46. Huang N, Zhai L, Couptry DE, et al. Multiple-component covalent organic frameworks. *Nat Commun*. 2016;7:12325.
47. Jin E, Geng K, Lee KH, et al. Topology-templated synthesis of crystalline porous covalent organic frameworks. *Angew Chem Int Ed*. 2020;59(29):12162-12169.
48. Karak S, Kumar S, Pachfule P, Banerjee R. Porosity prediction through hydrogen bonding in covalent organic frameworks. *J Am Chem Soc*. 2018;140(15):5138-5145.
49. Leith A, Martin R, Mayers M, Kittikhunnatham P, Larsen W, Shustova B. Confinement-guided photophysics in MOFs, COFs, and cages. *Chem Soc Rev*. 2021;50(7):4382-4410.
50. Li J, Wang J, Wu Z, Tao S, Jiang D. Ultrafast and stable proton conduction in polybenzimidazole covalent organic frameworks via confinement and activation. *Angew Chem Int Ed*. 2021;60(23):12918-12923.
51. Jin E, Asada M, Xu Q, et al. Two-dimensional sp<sup>2</sup> carbon-conjugated covalent organic frameworks. *Science*. 2017;357(6352):673-676.
52. Song X, Liu J, Zhang T, Chen L. 2D conductive metal-organic frameworks for electronics and spintronics. *Sci China Chem*. 2020;63(10):1391-1401.
53. Chen X, Li Y, Wang L, et al. High-lithium-affinity chemically exfoliated 2D covalent organic frameworks. *Adv Mater*. 2019;31(29):1901640.
54. Lin S, Diercks CS, Zhang YB, et al. Covalent organic frameworks comprising cobalt porphyrins for catalytic CO<sub>2</sub> reduction in water. *Science*. 2015;349(6253):1208-1213.
55. Wang L, Xu C, Zhang W, et al. Electrocleavage synthesis of solution-processed, imine-linked, and crystalline covalent organic framework thin films. *J Am Chem Soc*. 2022;144(20):8961-8968.
56. Song Y, Sun Q, Aguila B, Ma S. Opportunities of covalent organic frameworks for advanced applications. *Adv Sci*. 2019;6(2):1801410.
57. Bi S, Thiruvengadam P, Wei S, et al. Vinylene-bridged two-dimensional covalent organic frameworks via knoevenagel condensation of tricyanomesitylene. *J Am Chem Soc*. 2020;142(27):11893-11900.
58. Bi S, Yang C, Zhang W, et al. Two-dimensional semi-conducting covalent organic frameworks via condensation at arylmethyl carbon atoms. *Nat Commun*. 2019;10:2467.
59. Fan H, Mundstock A, Feldhoff A, et al. Covalent organic framework-covalent organic framework bilayer membranes for highly selective gas separation. *J Am Chem Soc*. 2018;140(32):10094-10098.
60. Kim H, Rao SR, Kapustin EA, et al. Adsorption-based atmospheric water harvesting device for arid climates. *Nat Commun*. 2018;9:1191.
61. Nguyen L, Hanikel N, Lyle J, Zhu C, Proserpio M, Yaghi M. A Porous covalent organic framework with voided square grid topology for atmospheric water harvesting. *J Am Chem Soc*. 2020;142(5):2218-2221.
62. Sick T, Rotter JM, Reuter S, et al. Switching on and off interlayer correlations and porosity in 2D covalent organic frameworks. *J Am Chem Soc*. 2019;141(32):12570-12581.

63. Wang P, Chen X, Jiang Q, et al. High-precision size recognition and separation in synthetic 1D nanochannels. *Angew Chem Int Ed.* 2019;58(44):15922-15927.
64. Liu M, Xu Q, Miao Q, et al. Atomic Co-N<sub>4</sub> and Co nanoparticles confined in COF@ZIF-67 derived core-shell carbon frameworks: bifunctional non-precious metal catalysts toward the ORR and HER. *J Mater Chem A.* 2022;10(1):228-233.
65. Li Q, Wang YC, Zeng J, et al. Bimetallic chalcogenides for electrocatalytic CO<sub>2</sub> reduction. *Rare Met.* 2021;40(12):3442-3453.
66. Wang J, Li P, Cui F, et al. A review of non-noble metal-based electrocatalysts for CO<sub>2</sub> electroreduction. *Rare Met.* 2021;40(11):3019-3037.

## SUPPORTING INFORMATION

Additional supporting information can be found online in the Supporting Information section at the end of this article.

**How to cite this article:** Liu M, Liu S, Xu Q, et al. Dual atomic catalysts from COF-derived carbon for CO<sub>2</sub>RR by suppressing HER through synergistic effects. *Carbon Energy.* 2023;1-12.  
[doi:10.1002/cey2.300](https://doi.org/10.1002/cey2.300)